A novel method for metal oxide deposition on carbon aerogels with potential application in capacitive deionization of saline water

M. C. Zafra[a], P. Lavela[a,*], G. Rasines[b], C. Macías[b], J. L. Tirado[a], C.O. Ania[c]

[a] Laboratorio de Química Inorgánica, Universidad de Córdoba, Marie Curie, Campus de Rabanales, 14071 Córdoba, Spain.

[b] Nanoquimia S.L., PCT Rabanales 21, Edf. Aldebarán M.4.7, Córdoba 14014 Córdoba, Spain.

[c] Instituto Nacional del Carbón (INCAR, CSIC), Apartado 73, 33080 Oviedo, Spain.

Abstract

Carbon aerogels doped with manganese or iron oxides were prepared by the resorcinol-formaldehyde method as potential electrodes for the capacitive deionization of sodium chloride from saline water. The solution containing the metal precursors was mixed with the hydrogel before the supercritical drying step ensuring a highly homogeneous dispersion of the nanometric metal oxides as determined by X-ray diffraction and electron microscopy. XPS spectra revealed the increased contribution of hydroxyl and carboxylic groups after the activation process. Also, an enhanced metal oxidation at the outer particle surface was observed. Nitrogen isotherms have revealed a decrease of the pore volume in doped samples ascribed to the partial blocking of the pore structure by the embedded nanometric metal oxide particles. Capacitance values as large as 99 F/g and 91 F/g were respectively recorded for CAGDFeAct and CAGDMnAct from by cyclic voltammetry. The large capacitance detected for the iron containing activated aerogel was confirmed by deionization experiments. An electrosorption capacity of 0.133 mmol/g was recorded for CAGDFeAct in a 0.025 M NaCl solution when 1.5 v were applied during the charge period. The study of the kinetic response of the electrodes showed a poor behavior for CAGDMnAct and correlated to the partial blocking of pore structure exerted by the embedded nanometric metal oxide particles.

Keywords: Carbon; Aerogel; Capacitive deionization; Voltammetry

*Corresponding author. Tel/Fax: 34957218637. E-mail address: iq1lacap@uco.es (P. Lavela)

1. Introduction

The electro-assisted adsorption of dissolved ions on the surface of a charged electrode is a promising technology for water desalination [1-6]. The dissolved ionic species are attracted to the surface of charged electrodes forming an electrical double layer (EDL), while a more diluted solution is eluted. The adsorbed ions can be further released when the charge induced on the electrodes is cancelled and simultaneously the energy employed to create the electrode/ electrolyte interface can be recovered [7-8]. This capacitor performance developed by these devices favorably contributes, at least theoretically, to the economic feasibility of the process. However, some drawbacks such as charge inefficiencies during the charge/discharge cycling must be resolved [9, 10]. Nanoporous carbon materials are characterized by a high surface area and enhanced microporosity, good electrical conductivity, and suitable electrochemical stability. These properties promote a high adsorption capacity in both single and multicomponent electrolytes [11, 12]. A large variety of carbon materials are currently researched for their applicability in water deionization including activated carbon [13], carbon nanofiber [14], and carbon nanotubes [15], graphene [16].

Carbon aerogels seem to be among the most promising nanoporous materials for capacitive water deionization (CDI). Previous reports have demonstrated that the adsorption properties of these carbon materials can be improved by tailoring their microstructural properties to the characteristics of the ion to be removed [17, 18].

Fortunately, the sol-gel polymerization method allows controlling a number of parameters as the resorcinol/catalyst (RC) ratio, gelification pH, pyrolysis and activation conditions, etc. [19, 20]. A current matter of research is the incorporation of finely dispersed metal oxides to the carbon material. The effect on the microstructure, conductivity and performance has been extensively reported for applications such as catalytic activity [20], supercapacitor [21] and lithium batteries [22]. Nevertheless, only a few examples are known about the use of metal oxides to optimize the performance of high surface carbons employed in desalination purposes [23-27].

In this work, we propose a novel method of incorporating manganese and iron oxide to carbon aerogels. The structural and morphological properties of the pyrolyzed and activated aerogels have been characterized by structural and spectroscopic techniques and the capacitive behavior has been elucidated by electrochemical and deionization experiments.

2. Experimental

2.1 Sample preparation

Two set of samples were synthesized by incorporating the manganese reagents at different stages of the aerogel preparation route. In both cases, carbon aerogel samples were prepared by the sol-gel polymerization method. Resorcinol (R) and formaldehyde (F) were dissolved in deionized water (W) and sodium carbonate as a catalyst (C). The molar ratios of reagents was set as R/C = 300; R/F = 0.5 and R/W = 0.06. To ensure a homogeneous mixture, the reagents were magnetically stirred in sealed glass moulds until gelification. This gel was aged in an oven at 40 °C for 24 h and then 70 °C for 120 h before a water-acetone exchange. In the first process, the gel was immersed in 200

mmol of acetone solution containing either $Mn(NO_3)_2 \cdot 6\ H_2O$ or $Fe(NO_3)_2 \cdot 9\ H_2O$ for 24 hours. Then, the doped gels were supercritically dried with CO_2 to preserve the pore structure of the polymerized gel. This aerogel was pyrolyzed at 750 °C for 2 hours under a N_2 stream. These samples were respectively named as CAGDMnPyr and CAGDFePyr. A second batch was subjected to activation by thermal treatment at 750 °C for 2 hours under CO_2 to provide an activated aerogel, named as CAGDMnAct and CAGDFeAct. For comparative purposes, non-doped pyrolyzed and activated aerogels were also prepared (CAGDPyr and CAGDAct). The chemical state at the surface of the electrode materials was analyzed by using X-ray Photoelectron Spectroscopy (XPS, SPECS Phobios 150MCD) with Mg K source and a chamber pressure of $4 \cdot 10^{-9}$ mbar. Thin film samples were subjected to high vacuum overnight.

2.2 Structural and textural characterization

X-Ray diffraction (XRD) patterns were recorded in a Siemens D5000 diffractometer equipped with a graphite monochromator and Cu Kα radiation operating at 40 kV and 30 mA. The samples were scanned between 10° and 70° (2θ) at a 0.04°/4 s scan rate. Scanning electron microscopy (SEM) images micrographs were obtained in a JEOL-SM6300. and transmission electron micrographs (TEM) in a PHILIPS CM-10 microscope. N_2 adsorption-desorption isotherms were measured at -196 °C in a (ASAP 2010, Micromeritics). The aerogels were previously outgassed under primary vacuum at 120 °C overnight. The pore size distributions were calculated by using the density functional theory (2D-NLDFT) approach [J. Jagiello, J. Kenvin, James P. Olivier, A. R. Lupini, C. I. Contescu, Using a New Finite Slit Pore Model for NLDFT Analysis of Carbon Pore Structure Adsorpt. Sci.Technol., 2011, 29,769-780]; the micropore volume was also evaluated by the DR method.

2.3 Electrochemical response of the carbon aerogels

The electrochemical response of the samples was measured on working electrodes consisting of both powdered material and monoliths. Powdered electrodes were prepared by mixing the aerogel (80%), Superior graphite (10%) and PVDF binder (10%). To ensure the homogeneity of this mixture a slurry in N-methyl pyrrolidone was prepared and spread on a titanium support and eventually dried at 70°C overnight. The working electrodes were cut in 13 mm disks and soaked in the electrolyte to ensure their impregnation in 0.1 M NaCl solution. Then, they were assembled in three electrode Swagelok^{TM} type cells with graphite current collectors. A Hg/Hg_2SO_4 and a platinum wire were respectively used as reference and counter electrode. The electrochemical measurements were performed in a Biologic VMP multichannel potentiostat. Cyclic voltammograms were recorded by cycling the cell between -0.5 and +0.5 V versus the reference electrode at different sweep rates (0.5 to 10 mV/s). Chronocoulometric curves were measured by subjecting the cell to a potentiostatic pulse of 300 mV vs Hg/Hg_2SO_4 for 120 s and recording the transient current. The internal impedance of the electrodes was measured by Electrochemical impedance spectroscopy (EIS). A modulated AC voltage signal of 5 mV versus equilibrium potential was applied to the cell over the frequency range 25 kHz to 10 mHz. The spectra were recorded in an Autolab PGSTAT12 system.

Capacitive deionization experiments were performed in a symmetric cell assembled with two monolithic aerogel electrodes. The monoliths were cut in 1 cm^2 pieces, polished and washed in deionized water for 30 minutes and then were vacuum impregnated with the electrolyte. Then, the electrodes were assembled in a batch cell containing 8.5 mL using titanium current collectors and Whatman glass GF/A fiber sheets as a separator. Sodium chloride solution with 0.025, 0.05 and 0.1 M

concentration were used as electrolytes. The experiments were performed under continuous stirring to avoid mass transfer restrictions from the bulk solution. The deionization experiment was carried out by applying a potentiostatic pulse of 0.9, 1.2 and 1.5 V for 150 min. The voltage pulse was applied using an Arbin potentiostat and current relaxation curves were recorded with the same instrument. The conductivity of the electrolyte was monitored by using a Crison GLP 31 conductivity meter (± 0.01 mS/cm). The electrosorption capacity was calculated as the molar concentration of adsorbed salt per mass of electrodes using the following equation:

$$M = (C_0\text{-}C)V\ /m \qquad [1]$$

being C_0 the initial molar concentration of salt solution, C is the concentration after adsorption (mol/L), V is the volume of solution (mL) and m is the mass of the monoliths (g) [26]. C and C_0 values were calculated from a calibration pattern considering the conductivity of the NaCl solutions with known concentrations [28].

3. Results and discussion

3.1. Structural characterization of the aerogels and chemical analysis.

XRD patterns of non-doped aerogels are characterized by two broadened bands located at ca. 22 and ca. 44 °(2θ) ascribable to the (002) and (100) reflections of graphite, respectively (Fig. 1). These profiles are commonly observed in disordered carbons annealed at temperatures beneath 1000 °C. Aerogels doped with manganese showed additional peaks which were unequivocally assigned to the (111) (200) and (220) reflections of MnO (JCPDS 07-0230). The contribution of these peaks to the pattern was more evident for the activated aerogel. Most likely, the annealing treatment

during the activation reaction is responsible for the enhancement of the crystallinity effect. In turn, iron doping led to the appearance of one large reflection at ca. 44.7° in CAGDFePyr, which was indexed to the (111) reflection of metallic iron (JCPDS 06-0696). A new set of reflections is observed in CAGDFeAct ascribable to the presence of magnetite Fe_3O_4 (JCPDS 19-0629) by partial oxidation of iron in the oxidizing conditions of the activation reaction.

XPS spectra for the C1s core level are depicted in figures 2a, b and 3 a, b. The overall profile recorded for CAGDMnPyr was decomposed in five Gaussian components (Fig. 2 a, b). A large peak appears at ca. 284.6 eV which is commonly attributed to aromatic and aliphatic carbon (sp^2) building the graphitic structure. A shoulder at ca. 286.0 eV is assigned to C–OH bonds. The long tail at high binding energies was decomposed in three small components at 287.9, 289.8 and 292.3 eV. According to the literature, they were respectively ascribed to double C=O bonds in carbonyl groups, carboxylic and shake-up satellite peaks due to π–π^* transitions in aromatic rings [29, 30]. The activation reaction involved an abrupt change in the spectrum profile. Thus, the signals at 286.4 and 290.2 eV, respectively ascribed to hydroxyl and carboxylic groups increase their contribution to the overall spectrum. These changes in the spectrum can be related to the effect of CO_2 on the carbon aerogel surface during the activation reaction. Similar changes were observed in the C1s XPS spectra recorded for the iron doped carbon aerogel (Fig. 3 a, b). The O1s spectra revealed three peaks (Fig. 2 c, d and. 3 c, d). The component at ca. 530.5 eV is assigned to the contribution of oxide anions existing in the metal oxide particles [29]. Otherwise, oxygen atoms in C-OH groups are responsible for the large signal at 533.3 eV [30]. Eventually, a third broadened signal at 536.6 eV could be ascribed to chemisorbed oxygen and/or water. The most remarkable change in the spectrum profiles after

activation resides in the increase of the contribution of the signal attributed to hydroxyl groups. The presence of the transition metal is revealed in the Mn2p core level spectra (Fig. 2e, f). The $2p_{3/2}$ and $2p_{1/2}$ signals respectively appear at ca 642 and 653.5 eV. These values are close to those expected for tetravalent Mn in MnO_2. Contrarily, the presence of a third satellite signal for CADMnPyr indicates that manganese atoms are only partially oxidized after pyrolysis [31]. For the iron doped aerogel, similar spectra were recorded for both pyrolyzed and activated samples (Fig. 3e, f). Two peaks appear at 711.4 and 723.8 eV ascribable to trivalent iron, which are preserved after activation. These results differ from those observed in the XRD patterns in which the presence of metallic iron, Fe_3O_4 and MnO were clearly discerned. The low depth of penetration of the X-Ray beam in XPS measurements can be responsible of detecting an amorphous and highly oxidized metal oxide phase on the particle surface, which contribution is negligible to the XRD patterns.

3.2. Textural characterization of the aerogels

TEM images of the activated aerogels clearly evidence the mesoporous structure built by the mutual aggregation of nanometric carbon particles (Fig. 4). The void spaces existing among these nanograins facilitate the migration of the ionic species towards the smallest micropores. The incorporation of metal oxides is evidenced by the presence of dark particles embedded in the carbon matrix. Thus, iron oxide appears as cubic nanometric particles which size is beneath 100 nm. Otherwise, MnO nanoparticles with size lower than 20 nm were observed in CAGDMnAct. In both cases, metal oxide particles are homogeneously dispersed through the carbon aerogel matrix. A semiquantitative EDS analysis showed a mass percentage of the metallic element of 2% for pyrolyzed and 4% for activated samples. The increased metal content detected after

the activation reaction can be ascribed to partial carbon burn off during the thermal treatment.

Nitrogen adsorption isotherms of the studied aerogels, recorded at -196 °C, are shown in Fig. 5 and 6. These isotherms can be classified type IV, according to the BDDT classification. The presence of microporosity is revealed by the large gas uptake at relative pressures below 0.2 for all the samples, while the hysteresis loops at relative pressures above 0.6 clearly show the presence of mesoporosity. CAGDPyr displays a broad distribution of mesopores with a maximum centered at around 22 nm. While the iron doping did not modify this pattern, the incorporation of manganese oxide brought about a slight narrowing of the mesoporosity (inset in Fig 5), as seen by the shift in the position of the hysteresis loop towards lower relative pressures. Furthermore, AGDMnPyr displays a bimodal distribution of mesopores with two clear maxima at 17 and 21 nm; this suggests the occurrence of pore blocking effects at the entrance of the mesopores upon Mn-doping. The larger size of the manganese oxide particles compared to those of iron (see Fig. 4) may explain this behavior. Data shown in Table 1 showed small variation in the surface area for the aerogels with values ranging from 665 to 750 m2/g; in contrast, the total pore volume follows a different trend, with smaller values for the metal-doped samples (beyond the dilution mass effect). This indicates that the metallic species do not provide additional porosity to the resulting metal-doped composite. After the activation in CO_2 atmosphere, the surface area values increased for all samples with the corresponding increase in the micropore and mesopore volumes. All three activated samples showed similar PSD irrespective of the metallic doping; compared to their corresponding pyrolyzed counterparts, the activation provoked a broadening of the mesoporosity, with PSD curves showing a significant contribution of pores between 25-30 nm.

3.3. Electrochemical response of the electrodes

Cyclic voltamograms of pyrolyzed and activated aerogels, recorded at 0.5 mV/s in the presence of 0.1 M NaCl solution, are displayed in figure 7. The accumulation of charge at the electric double layer interface when ions are adsorbed is responsible for the typical box-shape hysteresis [32]. Otherwise, pseudo-faradic reactions cannot be discarded as revealed by the occurrence of anodic current feature at potentials above +200 mV vs. Hg/Hg_2SO_4 [33]. A capacitance value of 68 F/g was recorded for CAGDPyr, while 72 and 79 F/g were measured for both CAGDFePyr and CAGDMnPyr. Likely, this significant increase of capacitance should be correlated to the pseudo-capacitive behavior exerted by the metal oxides. The larger increase of capacitance observed for the manganese containing sample may arise from the increase of the surface area observed for that sample. The effect of the activation post-treatment was to increase the capacitance values in all cases. Thus, values of 88, 99 and 91 F/g were respectively measured for CAGDAct CAGDFeAct and CAGDMnAct. These results clearly evidence the combination of iron doping during the pyrolysis reaction along an activation post-treatment optimize the adsorption capacity of the carbon aerogels.

Chronocoulometric relaxation provides interesting information about the kinetic response of the carbon aerogel electrodes (Fig. 8). The charge values plotted in the vertical axis have been normalized for comparative purposes. Non-activated samples evidenced close similar relaxation curves which makes difficult to discern among them. To overcome this problem, a numerical calculation of the time constant was applied according to the procedure described elsewhere [34]. These values are written in Table 2. The lowest value was recorded for CAGDMnPyr while a longer time was measured

for the iron containing aerogel. These values agree well with the highest surface area observed for CAGDMnPyr which undoubtedly facilitates the adsorption of the ionic species. Concerning the activated aerogels, a significant decrease of the time constant was detected for CAGDAct and CAGDFeAct, while a notorious increase was observed for CAGDMnAct (80.1 s). This result evidences effect of the decrease of surface area of CAGDMnAct as compared to CAGDAct. Although the activation reaction involves the release of amorphous carbon filling inner pores, MnO particles may block the entrance of mesopores counterbalancing the effect of activation.

These results were evidenced by calculating the internal electrode resistance to the electrosorption process from the impedance spectra. The Nyquist plots for the pyrolyzed and activated samples are displayed in figure 9a. These plots can be fitted to an equivalent circuit allowing calculating the resistance values attributed to the electrode–electrolyte interface (Fig. 9b). The resistance of the electrolyte solution represents a negligible contribution to the overall electrode resistance which can be inferred from high-frequency response [34]. The profile recorded at intermediate and low frequencies can be decomposed in a semicircle followed by a straight line at low frequencies. The fitting of the spectra was based on the equivalent circuit included in Fig. 9b, assuming a mixed kinetic and charge transfer control [35]. The components can be described as follows: R_{el} is the electrolyte solution resistance, R_{pol} is the polarization impedance, W is the Warburg impedance, and CPE is a constant phase element is used to overcome the non-ideal behavior of the electrode. The main contribution to R_{pol} is typically ascribed to the ionic resistance in the narrow micropores. These values are included in Table 2. The recorded R_{pol} values followed a similar tendency that the time constants above mentioned what evidences the validity of both methods to discuss the kinetic response of the carbon aerogels. The removal of amorphous carbon by the

activation process is an effective method for decreasing the electrode resistance. Nevertheless, this positive effect is counterbalanced by the blocking effect exerted by manganese oxides nanoparticles which hindered the diffusion of ionic species.

Monoliths of CAGDFeAct and CAGDMnAct were assembled in a batch cell, as shown in Fig. 10, to perform deionization experiments. Fig 11 and 12 shows their electrosorptive capacities for a charge and discharge cycle measured at different electrolyte concentration and/or applied voltage. Also, the corresponding current relaxation curves have been included. Fig. 11 a and b evidence the higher electrosorption capacity of activated aerogel containing iron oxide than that of manganese. Thus, 0.11 mmol of NaCl were adsorbed per gram of monolith in CAGDMnAct after the charge period at 1.5 V. Otherwise, 0.133 mmol/g were recorded for CAGDFeAct in the same experimental conditions. This result confirms the higher capacitive performance of the iron containing activated aerogel. Also, the steeper increase of adsorbed species determined for the latter sample evidence the better kinetic response above mentioned as compared to CAGDMnAct. Otherwise, the pH value slightly increased to a constant value of 8.3 as the potential was applied. This fact can be attributed to OH^- anions generated at the cathode. It can be attributed to the reduction of dissolved oxygen from the influent. An increase of the electrolyte concentration led to an improvement of the electrosorption capacity of CAGDMnAct, reaching a value of 0.101 mmol/g after the charge period (Fig. 12a). It represents a significant increase from the 0.03 mmol/g recorded in Fig. 11a. The effectiveness of the presence of the transition metal compounds was evidenced by recording the capacitive deionization of CAGDPyr in 0.025 M NaCl at different voltages. From figure 12b, an electrosorption capacity of only 0.044 and 0.061 mmmol g-1 were determined. These values are significantly lower than those recorded for CAGDFeAct, while the improvement induced by the presence

of MnO in CAGDMnAct was only detected for the experiments performed at 1.2 and 1.5 V. These results evidence the beneficial effect of the doping with transition metal oxides for activated carbon aerogel prepared in these conditions.

Charge efficiency was calculated as total salt adsorption over charge [10], and low values were obtained in all cases. These results can be attributed to the thickness of the monoliths and the occurrence of side reactions involving the reduction of dissolved oxygen and the increase of the pH value. In fact, a value of 0.4 was recorded for CAGDFeAct charged at 0.9 V which decreased to 0.29 at 1.5 V. An opposite effect was observed when the electrolyte concentration was increased. Thus, an increase of the efficiency from 0.27 to 0.49 was observed for CAGDMnAct when the electrolyte was concentrated from 0.025 M to 0.1 M.

4. Conclusions

Carbon aerogels doped with manganese or iron oxides were prepared by the resorcinol-formaldehyde method as potential electrodes for the electrosorption of sodium chloride from saline water. A novel method of doping has been reported here for the first time. The metal precursors were intimately mixed with the hydrogel before the supercritical drying step resulting in a highly homogeneous dispersion of the nanometric metal oxides. The microstructural characterization of the doped pyrolyzed aerogels revealed the presence of MnO and Fe nanoparticles. The activation process led to the partial oxidation to Fe_3O_4. XPS C1S and O1s spectra evidenced an increase of the contribution of hydroxyl and carboxylic groups after the activation process. Regardless of the pyrolyzed or activated samples, manganese and iron appears respectively at their tetravalent and trivalent state. This fact reveals that metal oxides are fully oxidized at

their outer surface. Nitrogen isotherms demonstrated the occurrence of a micro-mesoporous structure in the studied aerogels. The decrease of the pore volume observed in doped samples may involve the partial blocking of pore structure exerted by the embedded nanometric metal oxide particles.

Capacitance values recorded by cyclic voltammetry evidenced an increase from 68 F/g for CAGDPyr to 72 and 79 F/g for CAGDFePyr and CAGDMnPyr, respectively. This result can be ascribed to the pseudo-capacitive behavior exerted by the metal oxides. Even larger values were recorded for CAGDFeAct (99 F/g) and CAGDMnAct (91 F/g). The study of the kinetic response was carried out by the evaluation of the time constants and electrode polarization resistance derived from the chronocoulometric relaxation and impedance spectra, respectively. The data reveal an improvement of the kinetic properties of the electrodes after activation, excepting for the manganese containing aerogel. The blocking effect of nanometric MnO particles involving a decrease of the surface area can be responsible of this poor kinetic. These results were further evidenced by the capacitive deionization experiments which showed a significant improvement in the doped samples as compared to the pristine aerogel. Moreover, optimized properties were evidenced for CAGDFeAct. This carbon aerogel was able to adsorb 0.133 mmol/g in a 0.025 M NaCl solution when 1.5 V were applied during the charge period.

Acknowledgements

The authors are indebted to the MICINN (Contract IPT-2011-1450-310000 (ADECAR)) for the financial support. We also thank the fruitful collaboration of Isolux Ingeniería, S.A., Fundación Imdea Energia and Proingesa.

References

[1] M.S. Mauter, M. Elimelech, Environmental applications of carbon-based nanomaterials. Environ. Sci. Technol. 42 (2008) 5843-59.

[2] T Humplik, J Lee, S C O'Hern, B A Fellman, M A Baig, S F Hassan, M A Atieh, F Rahman, T Laoui, R Karnik, E N Wang, Nanostructured materials for water desalination, Nanotechnology 22 (2011) 292001.

[3] D. Qi., L. Zou, E. Hu, Electrosorption: an alternative option for desalination, Res. J. Chem. Environ. 11 (2007) 92-95.

[4] S. Porada, R. Zhao, A. van der Wal, V. Presser, P.M. Biesheuvel, Review on the Science and Technology of Water Desalination by Capacitive Deionization. Prog. Mater. Sci 58 (2013) 1388-1442.

[5] W. Huang , Y.M. Zhang, S.X. Bao, S.X. Song, Desalination by capacitive deionization with carbon-based materials as electrode: a review, Surf. Rev. Lett. 20 (2013) 1330003.

[6] M.A. Anderson, A.L. Cudero, J. Palma, Capacitive deionization as an electrochemical means of saving energy and delivering clean water. Comparison to present desalination practices: Will it compete?, Electrochim Acta. 55(2010) 3845-56.

[7] A. Subramani, M. Badruzzaman, J. Oppenheimer, J. G. Jacangelo, Energy minimization strategies and renewable energy utilization for desalination: A review. Water Res. 45 (2011) 1907-1920.

[8] S. Porada, L. Borchardt, M. Oschatz, M. Bryjak, J.S. Atchison, K.J. Keesman, S. Kaskel, P.M. Biesheuvel, V. Presser, Direct prediction of the desalination performance of porous carbon electrodes for capacitive deionization, Energ. Environ. Sci. 6 (2013) 3700-3712.

[9] S. Porada, M. Bryjak, A. van der Wal, P.M. Biesheuvel, Effect of electrode thickness variation on operation of capacitive deionization Electrochim. Acta 75 (2012) 148-156.

[10] P.M. Biesheuvel, S. Porada, M. Levi, M. Z. Bazant, Attractive forces in microporous carbon electrodes for capacitive deionization J Solid State Electrochem. On-line (2014) DOI 10.1007/s10008-014-2383-5.

[11] C. Tsouris, R. Mayes, J. Kiggans, K. Sharma, S. Yiacoumi, D. DePaoli, S. Dai, Mesoporous Carbon for Capacitive Deionization of Saline, Water. Environ. Sci. Technol. 45 (2011) 10243-10249.

[12] R. Zhao, M. van Soestbergen, H.H.M. Rijnaarts, A. van der Wal, M.Z. Bazant, P.M. Biesheuvel, Time-dependent ion selectivity in capacitive charging of porous electrodes, J.Colloid. Interf. Sci. 384 (2012) 38-44.

[13] M. Noked, A. Soffer, D. Aurbach, The electrochemistry of activated carbonaceous materials: past, present, and future, J Solid State Electrochem. 15 (2011) 1563-1578.

[14] G. Wang, C. Pan, L. Wang, Q. Dong, C. Yu, Z. Zhao, J. Qiu, Activated carbon nanofiber webs made by electrospinning for capacitive deionization, Electrochim. Acta 69 (2012) 65-70.

[15] P.S. Goh, A.F. Ismail, B.C. Ng, Carbon nanotubes for desalination: Performance evaluation and current hurdles, Desalination 308 (2013) 2-14.

[16] H. Wang, L.Y. Shi, T.T. Yan, J.P. Zhang, Q.D. Zhong, D.S. Zhang, Design of graphene-coated hollow mesoporous carbon spheres as high performance electrodes for capacitive deionization, J. Mater. Chem. A2 (2014) 4739-4750.

[17] G.P. Wu, J.B. Yang, D.P. Wang, R. Xu, K. Amine, C.X. Lu, A novel route for preparing mesoporous carbon aerogels using inorganic templates under ambient drying, Mater. Lett. 115 (2013) 1-4.

[18] M. Haro, G. Rasines, C. Macías C.O. Ania, Stability of Carbon gel electrode when used for electro-assisted removal of ions form brakish water, Carbon 49 (2011) 3723-3730.

[19] S.A. Al-Muhtaseb, J.A. Ritter, Preparation and properties of resorcinol-formaldehyde organic and carbon gels, Adv. Mater. 15 (2003) 101-14.

[20] G. Rasines, P. Lavela, C. Macías, M. Haro, C.O. Ania, J.L. Tirado. Electrochemical response of carbon aerogel electrodes in saline water, J. Electroanal. Chem. 671 (2012) 92-98.

[21] Y. Hardjono, H. Sun, H. Tian, C.E. Buckley, S. Wang, Synthesis of Co oxide doped carbon aerogel catalyst and catalytic performance in heterogeneous oxidation of phenol in water, Chem. Eng. J. 174 (2011) 376-382.

[22] Y. J. Lee, J. C. Jung, S. Park, J. G. Seo, S. H. Baeck, J. R. Yoon, J. Yi, I. K. Song, Preparation and characterization of metal-doped carbon aerogel for supercapacitor, Curr. Appl. Phys. 10 (2010) 947-951.

[23] P. Lavela, F. Nacimiento, G. F. Ortiz, J. L. Tirado, Sn–Co–C composites obtained from resorcinol-formaldehyde gel as anodes in lithium-ion batteries, J Solid State Electrochem. 14 (2010)139-148.

[24] L. Han, K.G. Karthikeyan, M.A. Anderson, J.J. Wouters, Kelvin B. Gregory. Mechanistic insights into the use of oxide nanoparticles coated asymmetric electrodes for capacitive deionization. Electrochim. Acta 90 (2013) 573-581.

[25] L. M. Chang, X. Y. Duan, W. Liu, Preparation and electrosorption desalination performance of activated carbon electrode with titania, Desalination 270 (2011) 285-290.

[26] J. Yang, L. Zou, H. Song, Z. Hao, Development of novel MnO_2/nanoporous carbon composite electrodes in capacitive deionization technology, Desalination 276 (2011) 199-206.

[27] H.J. Yin, S.L. Zhao, J.W. Wan, H.J. Tang, L. Chang, L.C. He, H.J. Zhao, Y. Gao, Z.Y. Tang, Three-Dimensional Graphene/Metal Oxide Nanoparticle Hybrids for High-Performance Capacitive Deionization of Saline Water, Adv. Mater. 25 (2013) 6270-6276.

[28] M.A. Tofighy, T. Mohammadi, Salty water desalination using carbon nanotube sheets, Desalination 258 (2010) 182-186.

[29] E.R. Edwards, E.F. Antunes, E.C. Botelho, M.R. Baldan, E.J. Corat, Appl. Surf. Sci. 258 (2011) 641-648.

[30] S. Biniak, G. Szymanski, J. Siedlewski, A. Swiatkowski, The characterization of activated carbons with Oxygen and nitrogen surface groups, Carbon, 35 (1997) 1799-1810.

[31] V. Di Castro, G. Polzonetti, XPS study of MnO oxidation, J. Electron. Spectrosc. Relat. Phenom. 48 (1989) 117-123.

[32] L.X. Li, L.D. Zou, H.H. Song, G. Morris, Ordered mesoporous carbons synthesized by a modified sol-gel process for electrosorptive removal of sodium chloride, Carbon 47 (2009) 775-781.

[33] M.C. Zafra, P. Lavela, C. Macías, G. Rasines, J.L. Tirado, Electrosorption of environmental concerning anions on a highly porous carbon aerogel, J. Electroanal. Chem. 708 (2013) 80-86.

[34] M. Noked, E. Avraham, A. Soffer, D.Aurbach, The Rate-Determining Step of Electroadsorption Processes into Nanoporous Carbon Electrodes Related to Water Desalination, J. Phys. Chem. C 113 (2009)21319–27.

[35] X.M. Liu, R. Zhang, L. Zhan, D.H. Long, W.M. Qiao, J.H. Yang, L.C. Ling, Impedance of carbon aerogel/activated carbon composites as electrodes of electrochemical capacitors in aprotic electrolyte New Carbon Mater. 22 (2007)153–8.

Table 1: BET surface area and pore volume values derived from the nitrogen isotherms measured for the doped and non-doped aerogel samples.

Sample	CAGDPyr	CAGDFePyr	CAGDMnPyr
S_{BET} / m^2 g^{-1}	693	663	750
V_{MICRO}[a] /cm^3 g^{-1}	0.16	0.15	0.17
V_{MESO} / cm^3 g^{-1}	1.24	1.19	1.12
V_{TOTAL}[b] / cm^3 g^{-1}	1.43	1.38	1.32

Sample	CAGDAct	CAGDFeAct	CAGDMnAct
S_{BET} / m^2 g^{-1}	848	850	841
V_{MICRO}[a] / cm^3 g^{-1}	0.22	0.20	0.20
V_{MESO} / cm^3 g^{-1}	1.39	1.46	1.35
V_{TOTAL}[b] / cm^3 g^{-1}	1.67	1.70	1.58

[a] Evaluated from DR equation.
[b] Evaluated at $p/p_o \sim 0.99$.

Table 2: Time constants (τ) calculated from the chronocoulometric curves and electrical resistances (R_{pol}) as derived from the fitted impedance spectra of the carbon aerogel electrodes according to the equivalent circuit included in figure 9b.

	τ / s	R_{pol} / $\Omega \times g$
CAGDPyr	62.9	0.72
CAGDFePyr	64.1	0.86
CAGDMnPyr	56.7	0.75
CAGDAct	53.3	0.58
CAGDFeAct	57.8	0.63
CAGDMnAct	80.1	1.24

Figure captions

Figure 1: X-ray diffraction patterns of pyrolyzed and activated carbon aerogels. Miller indexes for MnO (CAGDMnPyr, CAGDMnAct) and Fe_3O_4 reflections (CAGDFeAct , CAGDFePyr) have been included.

Figure 2: XPS spectra at the C1s, O1s and Mn2p core levels of a,c,e) CAGDMnPyr, and b,d,f) CAGDMnAct.

Figure 3: XPS spectra at the C1s, O1s and Fe2p core levels of a,c,e) CAGDFePyr, and b,d,f) CAGDFeAct.

Figure 4: TEM images of activated carbon aerogels a) CAGDFeAct and c) CAGDMnAct. Arrows indicate the presence of MnO and Fe_2O_3 particles.

Figure 5: N_2 adsorption isotherms at 77 K and PSD (inset) of the pyrolyzed carbon aerogels.

Figure 6: N_2 adsorption isotherms at 77 K and PSD (inset) of the activated carbon aerogels.

Figure 7: Cyclic voltammograms of a) pyrolyzed and b) activated carbon aerogels obtained recorded at 0.5 mV/s in 0.1 M NaCl solution.

Figure 8: Normalized chronocoulometric curves of a) pyrolyzed and b) activated carbon aerogels obtained after a pulse of 300 mV vs Hg/Hg_2SO_4 for 120 s in 0.1 M NaCl solution.

Figure 9: a) Nyquist plots derived from the impedance spectra recorded for the three electrode cells assembled with the pyrolyzed and activated carbon aerogel samples in 0.1 M NaCl solution. A modulated AC voltage signal of 5 mV versus equilibrium potential was applied; b) Equivalent circuit used for the fitting of the spectra. The spectra have been vertically shifted for a clear observation.

Figure 10: Schematic of the batch cell used for capacitive deionization experiments.

Fig. 11: Capacitive deionization experiments in 0.025 M NaCl of a) CAGDMnAct and b) CAGDFeAct at an applied voltage of 0.9, 1.2 and 1.5 V.

Fig. 12: Capacitive deionization experiments of a) CAGDMnAct at an applied voltage of 0.9 V in 0.025, 0.05 and 0.1 M NaCl solutions; b) CAGDPyr in 0.025 M NaCl at an applied voltage of 0.9, 1.2 and 1.5 V.

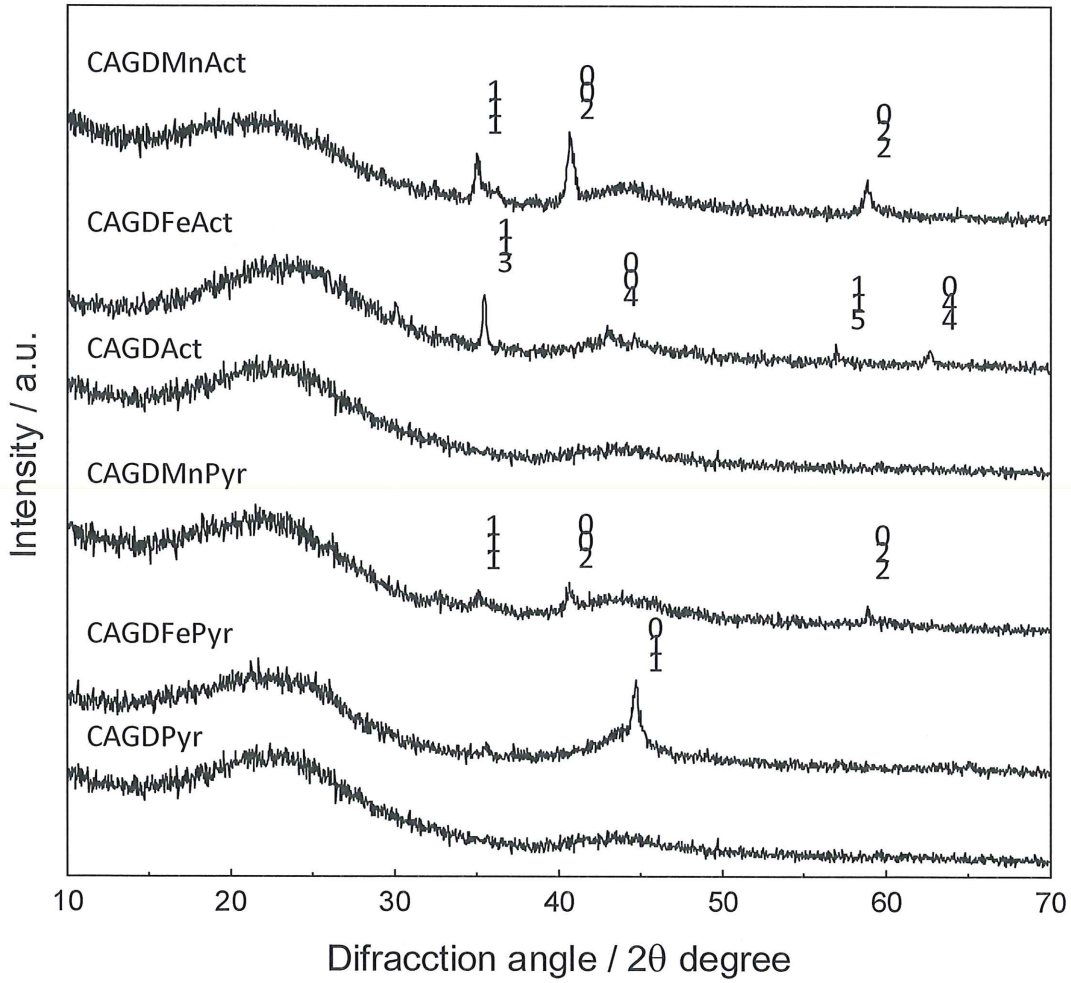
CAGDMnAct
CAGDFeAct
CAGDAct
CAGDMnPyr
CAGDFePyr
CAGDPyr
Intensity / a.u.
10
20
30
40
50
60
70
Difracction angle / 2θ degree

Figure 1

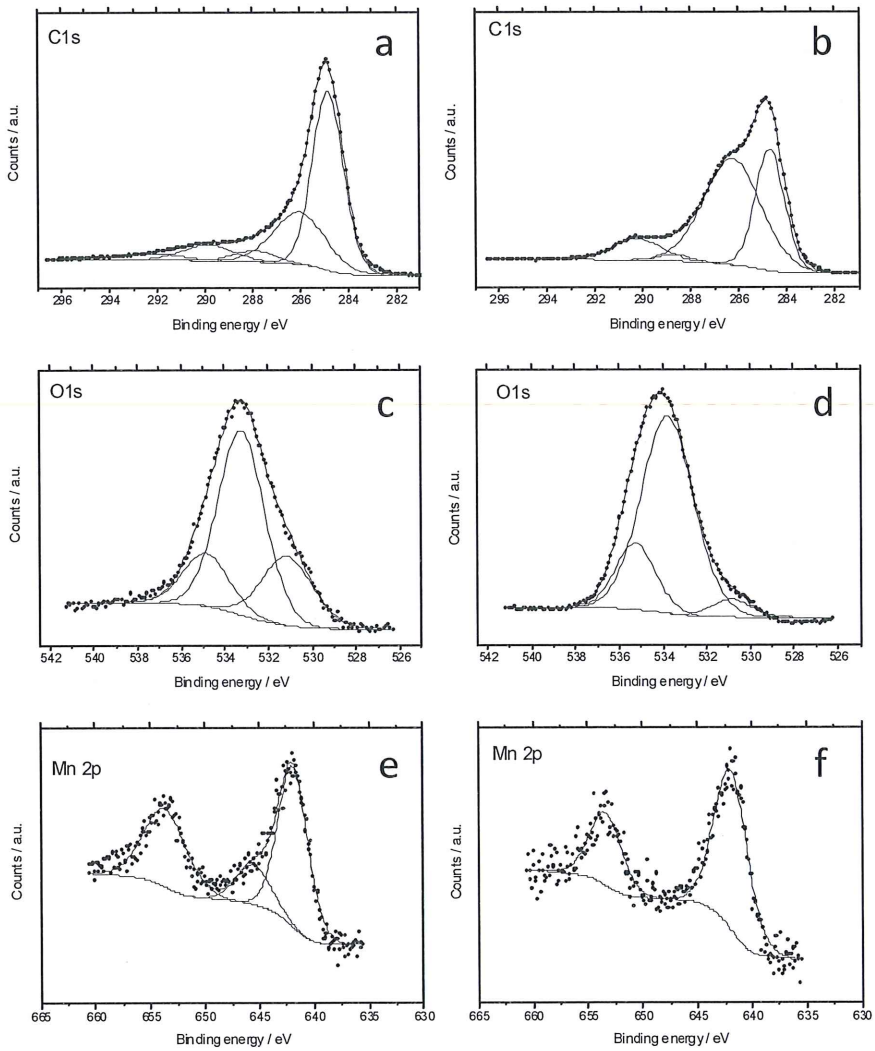
C1s
a
Counts / a.u.
296 294 292 290 288 286 284 282
Binding energy / eV
C1s
b
Counts / a.u.
296 294 292 290 288 286 284 282
Binding energy / eV
O1s
c
Counts / a.u.
542 540 538 536 534 532 530 528 526
Binding energy / eV
O1s
d
Counts / a.u.
542 540 538 536 534 532 530 528 526
Binding energy / eV
Mn 2p
e
Counts / a.u.
665 660 655 650 645 640 635 630
Binding energy / eV
Mn 2p
f
Counts / a.u.
665 660 655 650 645 640 635 630
Binding energy / eV

Figure 2

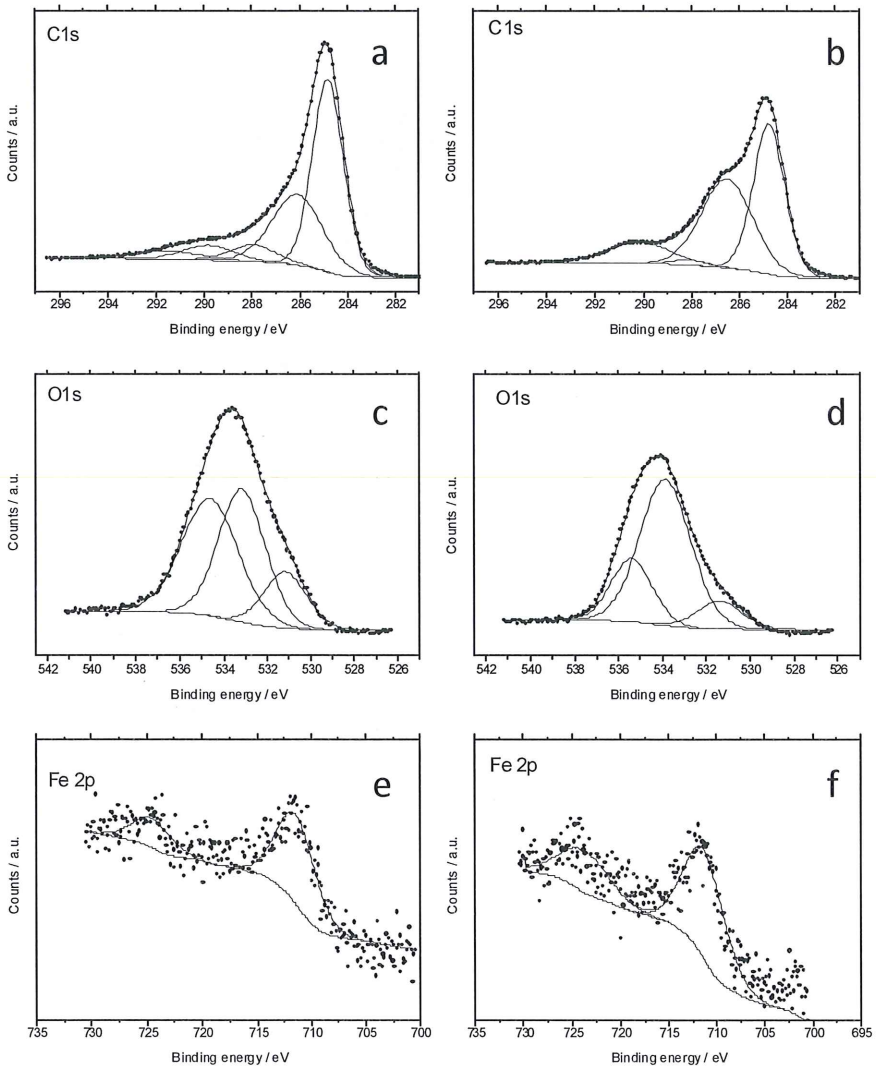
C1s
a
Counts / a.u.
296 294 292 290 288 286 284 282
Binding energy / eV
C1s
b
Counts / a.u.
296 294 292 290 288 286 284 282
Binding energy / eV
O1s
c
Counts / a.u.
542 540 538 536 534 532 530 528 526
Binding energy / eV
O1s
d
Counts / a.u.
542 540 538 536 534 532 530 528 526
Binding energy / eV
Fe 2p
e
Counts / a.u.
735 730 725 720 715 710 705 700
Binding energy / eV
Fe 2p
f
Counts / a.u.
735 730 725 720 715 710 705 700 695
Binding energy / eV

Figure 3

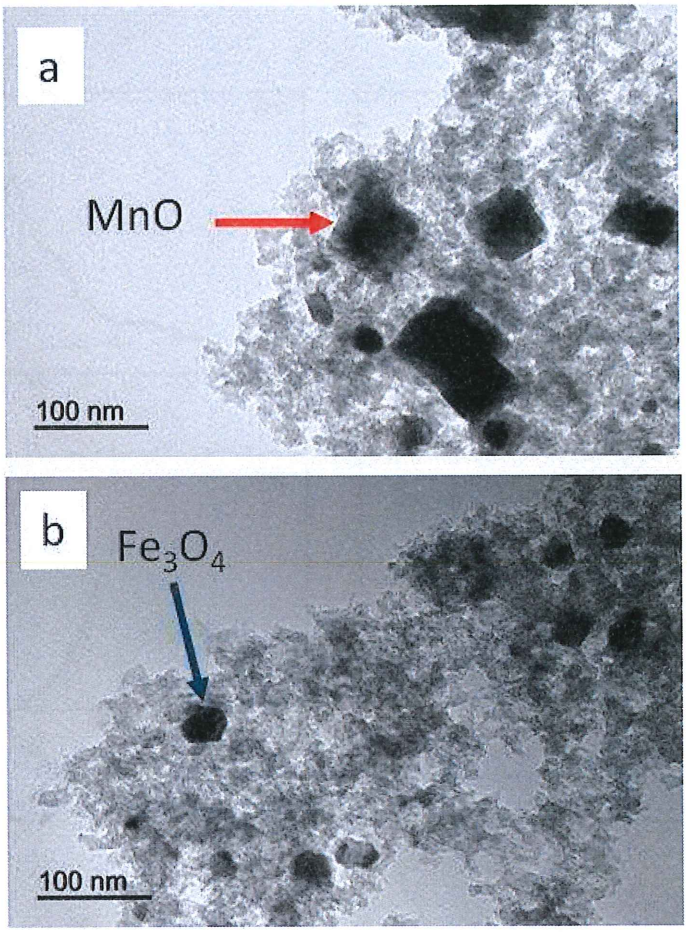

Figure 4

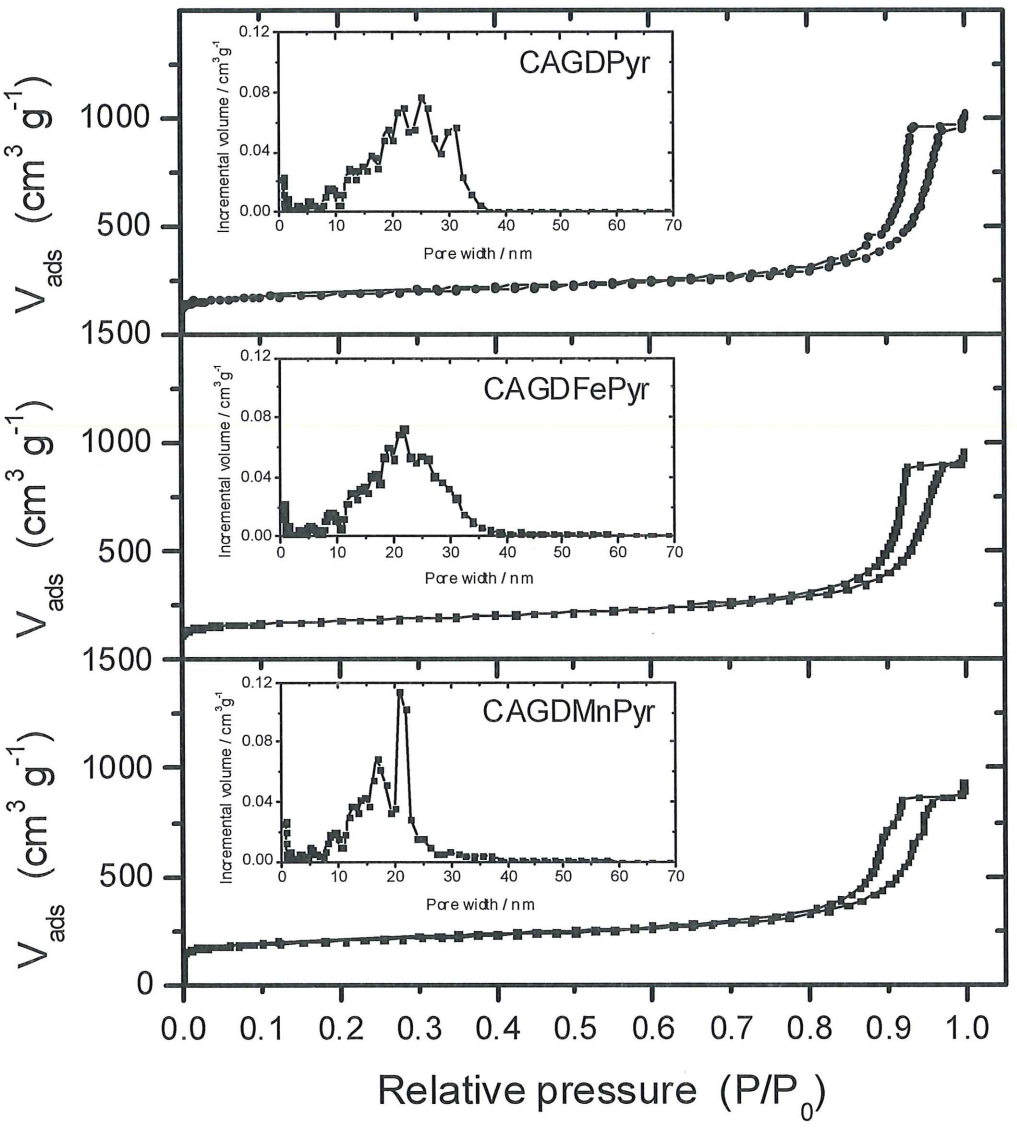
CAGDPyr
CAGDFePyr
CAGDMnPyr
Incremental volume / cm3g-1
Pore width / nm
Vads (cm3 g-1)
Relative pressure (P/P0)

Figure 5

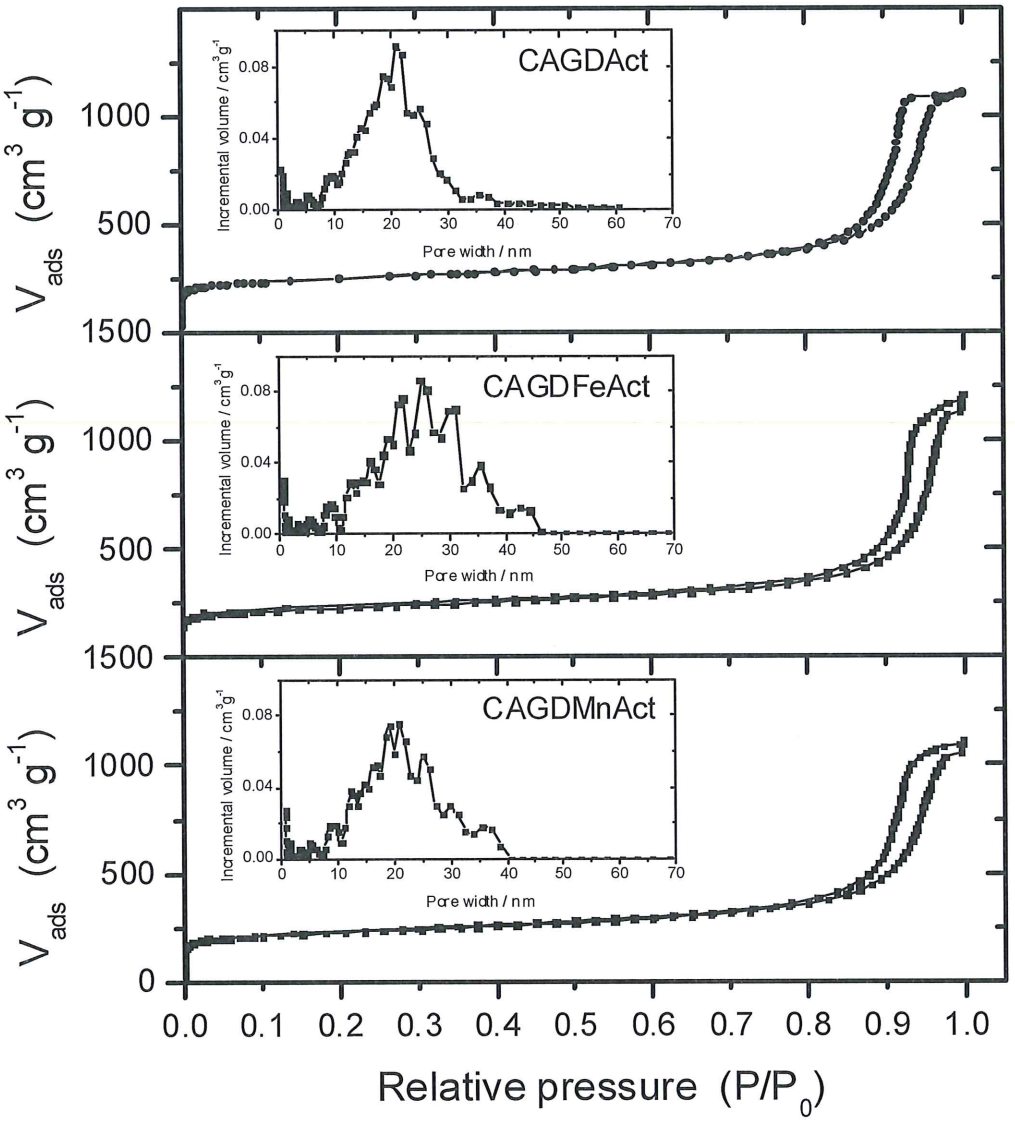
CAGDAct
CAGDFeAct
CAGDMnAct
Incremental volume / cm3g-1
Pore width / nm
Vads (cm3 g-1)
Relative pressure (P/P0)

Figure 6

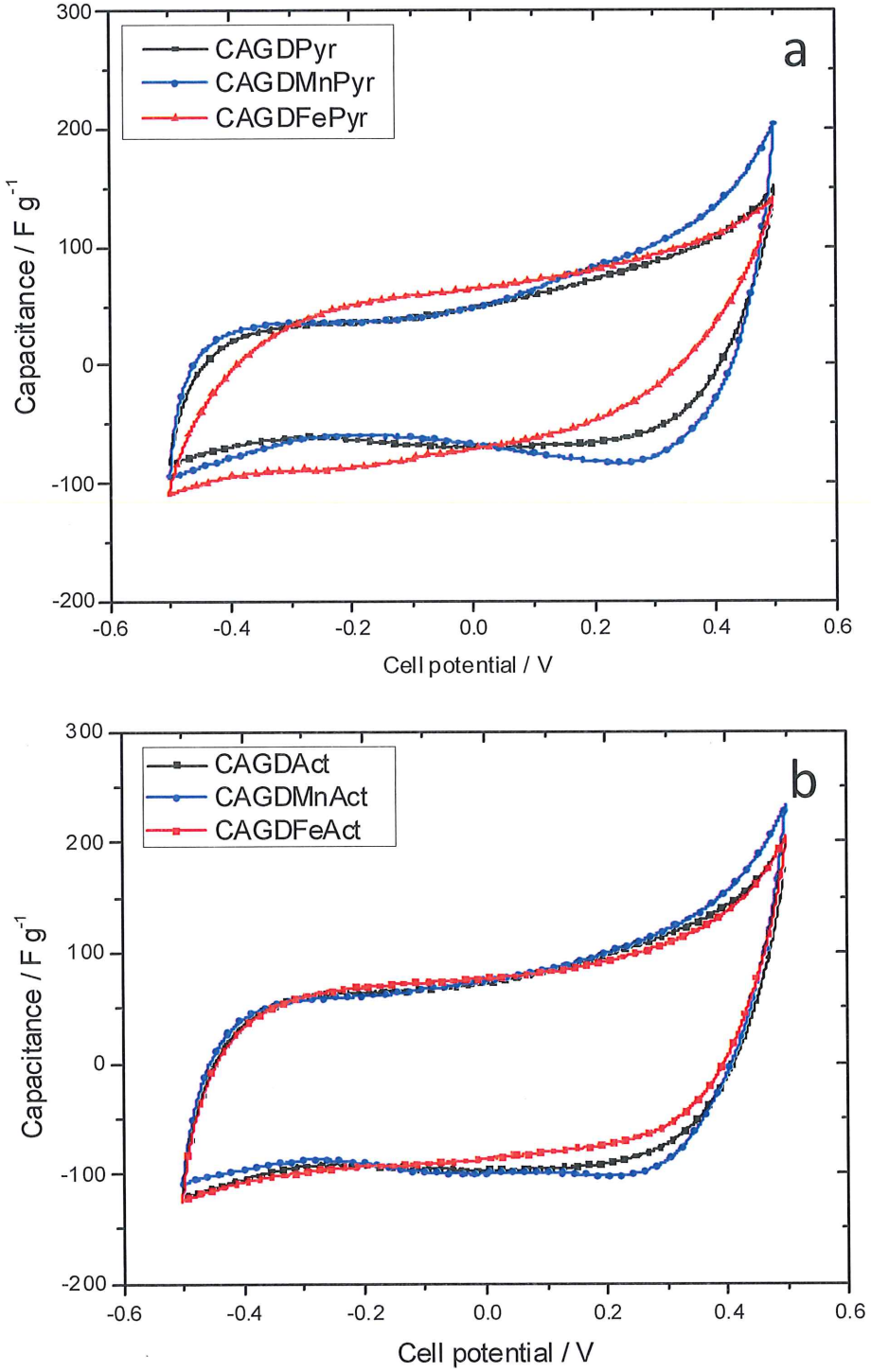
CAGDPyr
CAGDMnPyr
CAGDFePyr
a
Capacitance / F g-1
Cell potential / V
CAGDAct
CAGDMnAct
CAGDFeAct
b
Capacitance / F g-1
Cell potential / V

Figure 7

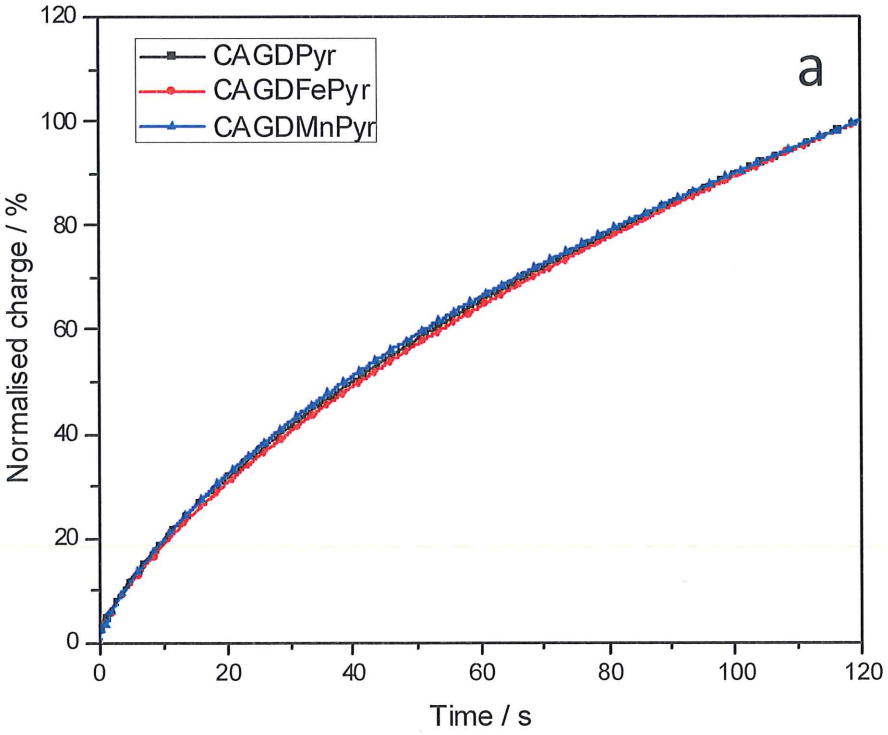
CAGDPyr
CAGDFePyr
CAGDMnPyr
a
Normalised charge / %
Time / s
0
20
40
60
80
100
120

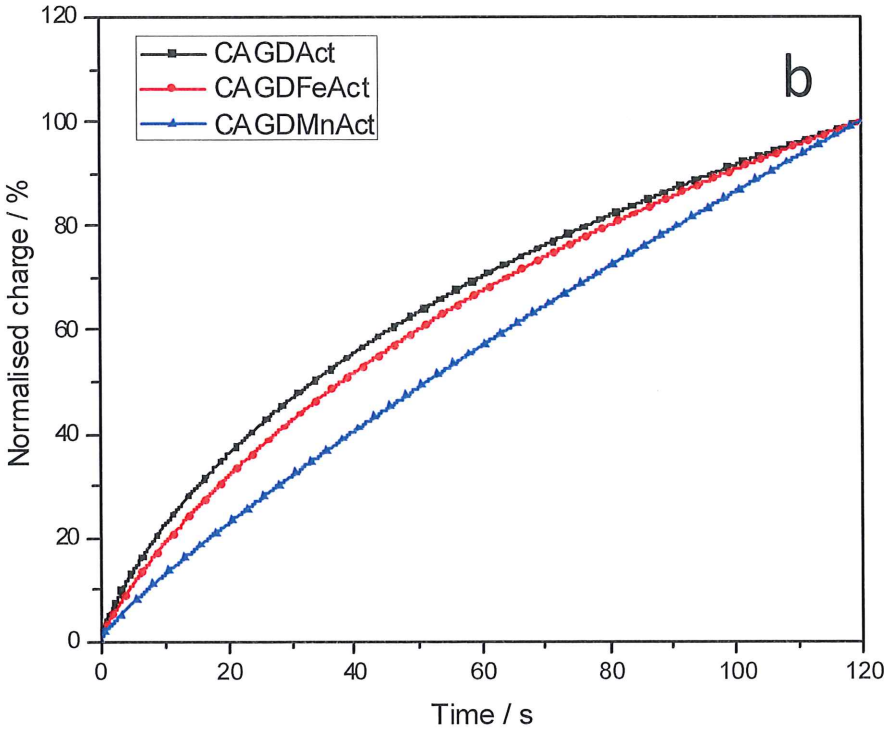
CAGDAct
CAGDFeAct
CAGDMnAct
b
Normalised charge / %
Time / s
0
20
40
60
80
100
120

Figure 8

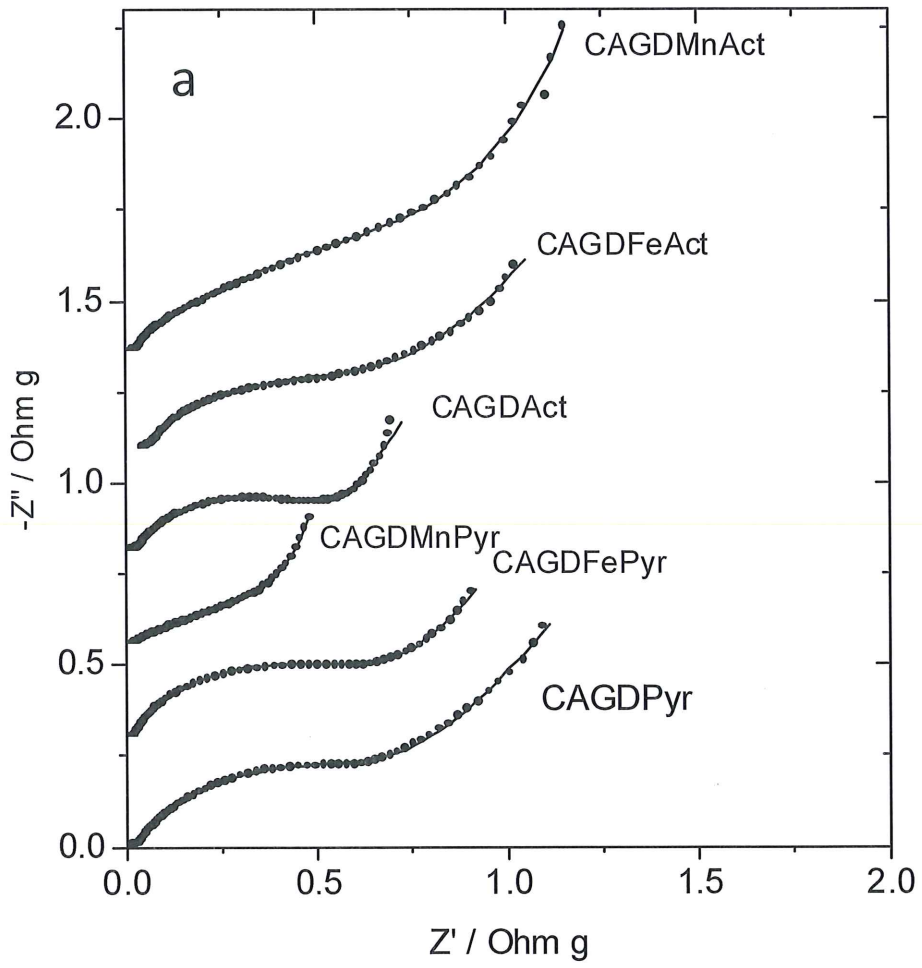
a
CAGDMnAct
CAGDFeAct
CAGDAct
CAGDMnPyr
CAGDFePyr
CAGDPyr
-Z'' / Ohm g
Z' / Ohm g
0.0
0.5
1.0
1.5
2.0

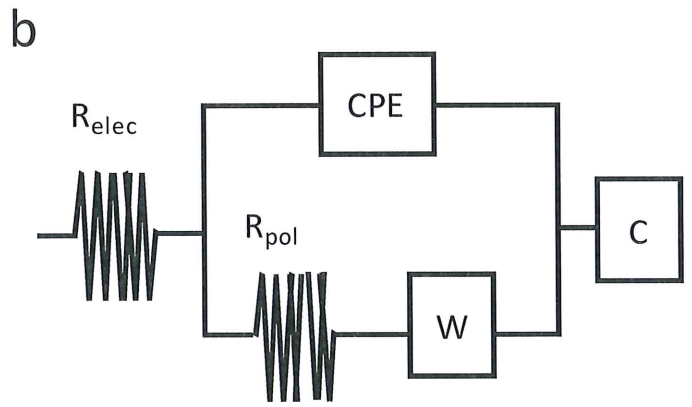
b
R_{elec}
CPE
R_{pol}
C
W

Figure 9

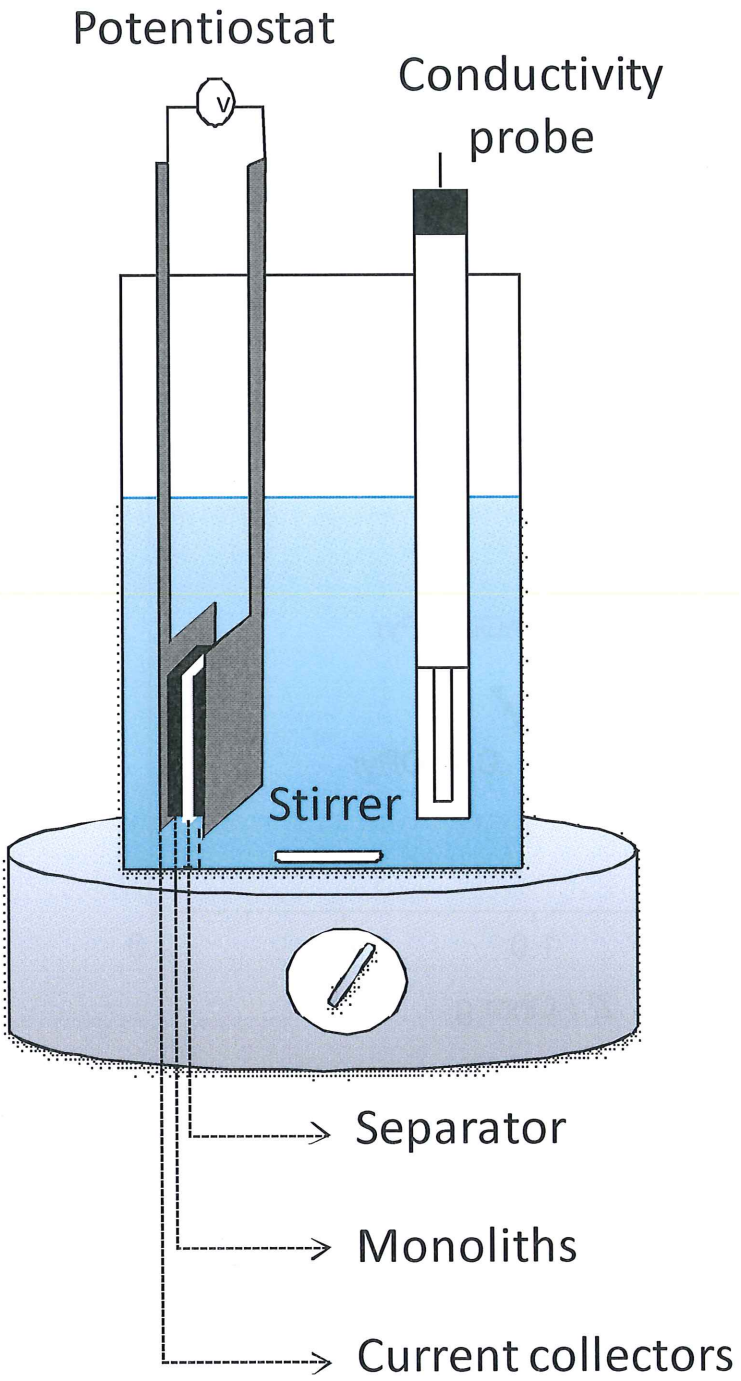
Potentiostat
V
Conductivity
probe
Stirrer
Separator
Monoliths
Current collectors

Figure 10

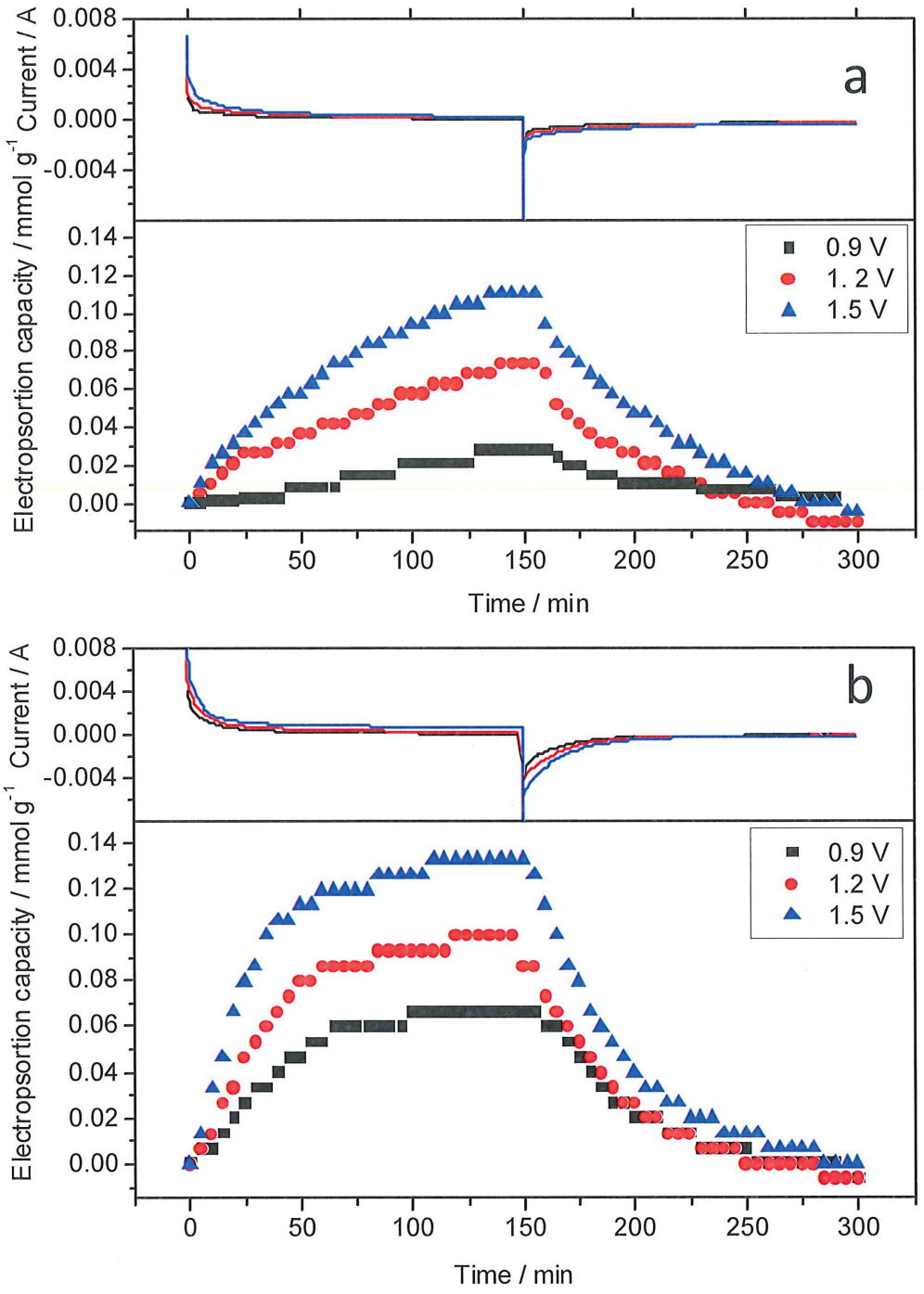
a
b
Current / A
Electropsortion capacity / mmol g-1
0.008
0.004
0.000
-0.004
0.14
0.12
0.10
0.08
0.06
0.04
0.02
0.00
0.9 V
1. 2 V
1.5 V
1.2 V
0
50
100
150
200
250
300
Time / min

Figure 11

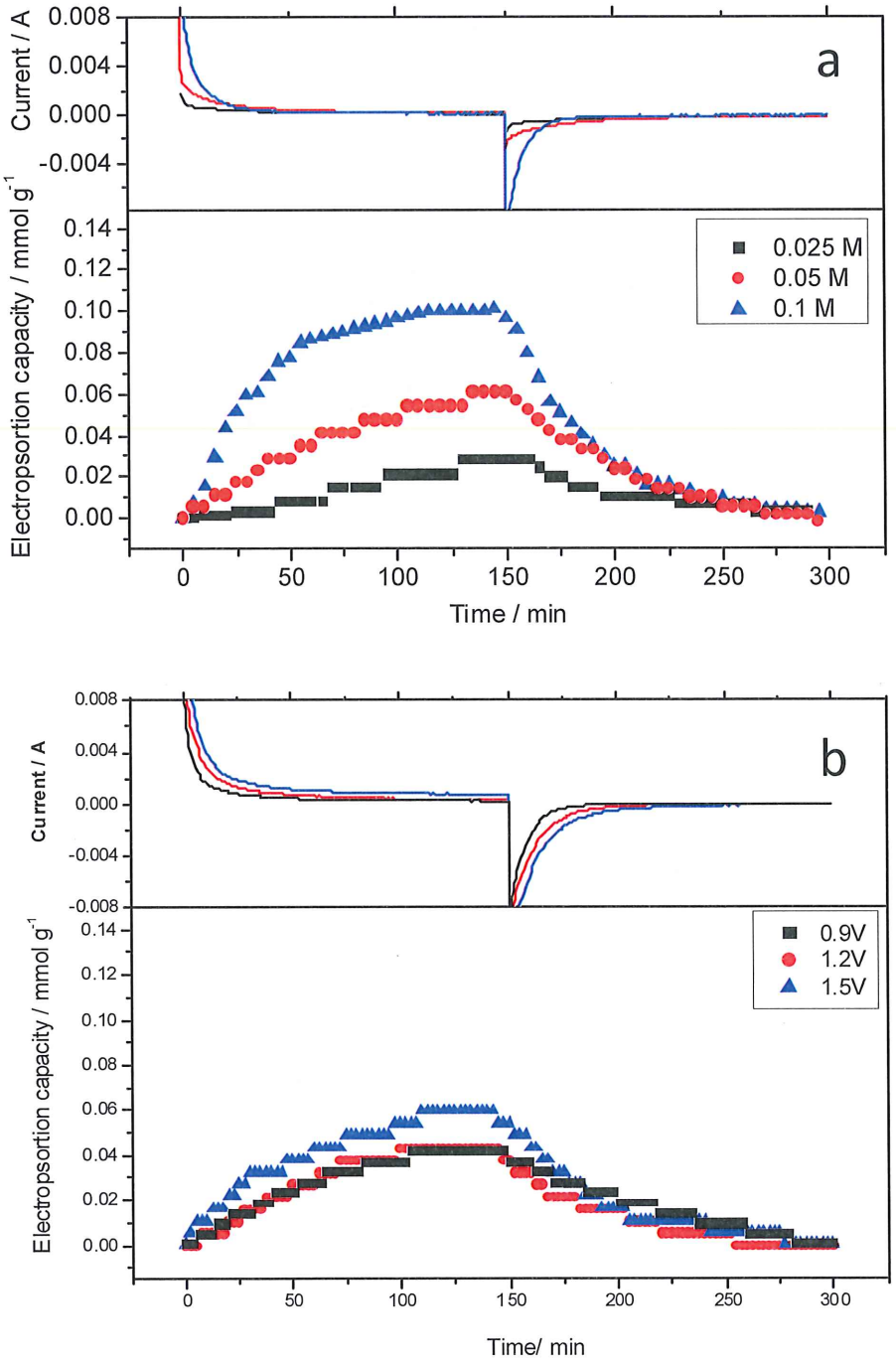
a
Current / A
0.008
0.004
0.000
-0.004
Electropsortion capacity / mmol g-1
0.14
0.12
0.10
0.08
0.06
0.04
0.02
0.00
0.025 M
0.05 M
0.1 M
0
50
100
150
200
250
300
Time / min
b
Current / A
0.008
0.004
0.000
-0.004
-0.008
Electropsortion capacity / mmol g-1
0.14
0.12
0.10
0.08
0.06
0.04
0.02
0.00
0.9V
1.2V
1.5V
0
50
100
150
200
250
300
Time/ min

Figure 12